

Exploring the evolution of circular polarized light backscattered from turbid tissue-like disperse medium utilizing generalized Monte Carlo modeling approach with a combined use of Jones and Stokes-Mueller formalisms

Ivan Lopushenko^{a,*}, Oleksii Sieryi^a, Alexander Bykov^a, Igor Meglinski^{a,b}

^aUniversity of Oulu, Opto-Electronics and Measurement Techniques Unit, Faculty of Information Technology and Electrical Engineering, P.O.Box 4500, Oulu, Finland, 90014

^bAston University, College of Engineering and Physical Sciences, Birmingham, UK, B4 7ET

Abstract.

Significance: Phase retardation of circularly polarized light (CPL), backscattered by biological tissue, is used extensively for quantitative evaluation of cervical intraepithelial neoplasia, presence of senile Alzheimer's plaques and characterization of biotissues with optical anisotropy. The Stokes polarimetry and Mueller matrix approaches demonstrate high potential in definitive non-invasive cancer diagnosis and tissue characterization. The ultimate understanding of CPL interaction with tissues is essential for advancing medical diagnostics, optical imaging, therapeutic applications, and the development of optical instruments and devices.

Aim: We investigate propagation of CPL within turbid tissue-like scattering medium utilizing a combined use of Jones and Stokes-Mueller formalisms in Monte Carlo (MC) modeling approach. We explore the fundamentals of CPL memory effect and depolarization formation.

Approach: The generalized MC computational approach developed for polarization tracking within turbid tissue-like scattering medium is based on the iterative solution of the Bethe-Salpeter equation. The approach handles helicity response of CPL scattered in turbid medium and provides explicit expressions for assessment of its polarization state.

Results: Evolution of CPL backscattered by tissue-like medium at different conditions of observation in terms of source-detector configuration is assessed quantitatively. The depolarization of light is presented in terms of the coherence matrix and Stokes-Mueller formalism. The obtained results reveal the origins of the helicity flip of CPL depending on the source-detector configuration and the properties of the medium, and are in a good agreement with the experiment.

Conclusions: By integrating Jones and Stokes-Mueller formalisms, the combined MC approach allows for a more complete representation of polarization effects in complex optical systems. The developed model is suitable to imitate propagation of the light beams of different shape and profile, including Gaussian, Bessel, Hermite-Gaussian, and Laguerre-Gaussian beams, within tissue-like medium. Diverse configuration of the experimental conditions, coherent properties of light and peculiarities of polarization can be also taken into account.

Keywords: Circularly polarized light, Monte Carlo, Stokes vector, Jones-Mueller approach, polarimetry, turbid tissue-like scattering medium.

*Address all correspondence to I. Lopushenko, ivan.lopushenko@oulu.fi

1 Introduction

Recent advances of the biomedical polarimetry have clearly demonstrated that circularly polarized light (CPL) can be effectively used for overall characterization of biological tissues with optical anisotropy¹⁻³ including detection of the senile Alzheimer's plaques^{4,5} and quantitative evaluation of the cervical intraepithelial neoplasia.^{6,7} Proper exploration of the CPL-tissue interaction requires accurate self-consistent descriptive simulation tools.^{1,8,9} Monte Carlo (MC) based approaches are widely recognized as efficient tools for analyzing light scattering by biological tissues and turbid medium.¹⁰⁻¹⁴ In biophotonics, MC methods like MCML¹⁵ created by L. Wang

43 and S. Jacques were originally designed to simulate scalar light transport within turbid scatter-
 44 ing medium^{16,17} and were fundamentally relying on the radiative transfer equation (RTE).^{18–20} As
 45 significant role of polarized light in extending diagnostic capabilities of biomedical tools became
 46 apparent,^{21,22} MC methods evolved accordingly resulting in many practical and popular tools par-
 47 ticularly developed by J. C. Ramella-Roman, S. Prahl and S. Jacques,^{23,24} A. H. Hielscher,^{25,26} L.
 48 Wang²⁷ and M. Xu.²⁸ Fundamental ground for these polarized MC approaches was established
 49 by the vector radiative transfer equation (VRTE) which represents a system of equations for each
 50 Stokes parameter and can be rigorously derived from the Maxwell electromagnetic theory.^{29–31} At
 51 the same time, an approach based on the iterative solution to Bethe-Salpeter (BS) equation^{19,32–34}
 52 utilizing Jones vector formalism has been demonstrated to be effective for polarization tracking of
 53 MC-photons within turbid tissue-like medium and simulation of coherent backscattering.^{13,14,35–39}
 54 Recently, it has been shown on the fundamental level that VRTE and BS based approaches are
 55 equivalent under certain conditions.⁴⁰ Advantages of the BS-based approach involve a direct re-
 56 lation to the analytic Milne solution and intuitive physical interpretation of the multiple scattering
 57 process via ladder diagrams.

58 Modern implementations of the polarization-resolved MC^{14,41} aim to provide a comprehensive
 59 description of polarized light scattering with either Jones or Mueller formalism, depending on the
 60 representation of the polarization state.⁴² Most interest is shown in CPL which, unlike linearly
 61 polarized light, possesses a unique sense of directional awareness allowing to determine if light
 62 was forward or backscattered due to its intrinsic angular momentum associated with helicity^{35,39,43}
 63 (see Fig. 1a). This peculiar property of CPL is a manifestation of anisotropy of scattering⁸ and
 64 is also known as polarization memory.^{44–46} Stokes vector polarimetry approach with the Poincaré
 65 sphere as a graphical tool is viewed as one of the most fitting instruments for light characterization
 66 with account for helicity (see Fig. 1b).

67 In this work we address the conservation of the polarization memory and penetration depth of
 68 the CPL scattered in turbid tissue-like medium. We introduce a Monte Carlo modeling approach

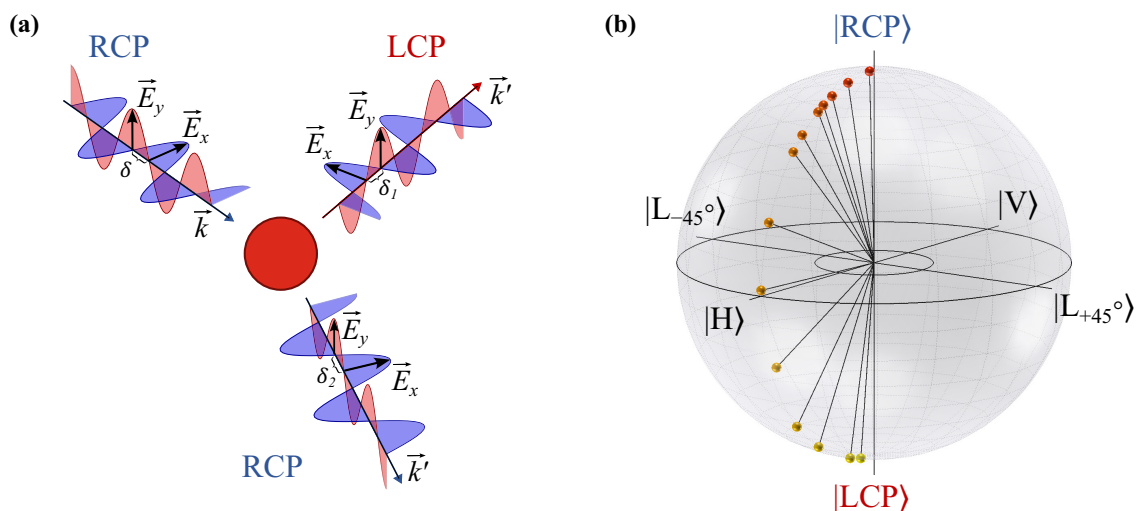


Fig 1 (a) Physics of the helicity flip: when right circularly polarized (RCP) light is scattered in forward direction its helicity is preserved, whereas for backscattered light its polarization state is changed to left circular polarization (LCP). (b) Degenerate polarization states $|H\rangle$, $|V\rangle$, $|L_{+45^\circ}\rangle$, $|L_{-45^\circ}\rangle$, $|RCP\rangle$, $|LCP\rangle$ (defined in Sec. 2.1) and helicity flip (polarization state crossing the equator) depicted on the Poincaré sphere.

69 specially developed to unify and generalize BS-based simulation of linearly, circularly and/or el-
70 liptically polarized light propagation. For the first time we express the BS-based Monte Carlo
71 model in terms of the Stokes-Mueller formalism and show that our approach efficiently allows to
72 compute Jones and Stokes vectors, Mueller matrix components and all degrees of polarization. We
73 explore the evolution of the CPL depolarization while propagating within turbid tissue-like scat-
74 tering medium and consider the dynamic binding of circular polarization memory with the helicity
75 flips occurring along the light path length within the medium.

76 2 Theory

77 2.1 Relation between Stokes and Jones formalism

78 Stokes vector is traditionally defined for the fully polarized light in the following form:⁴³

$$\begin{pmatrix} I_p \\ Q_p \\ U_p \\ V_p \end{pmatrix} = \frac{1}{2} \begin{pmatrix} E_x E_x^* + E_y E_y^* \\ E_x E_x^* - E_y E_y^* \\ E_x E_y^* + E_y E_x^* \\ j(E_x E_y^* - E_y E_x^*) \end{pmatrix}. \quad (1)$$

79 Here, j denotes the imaginary unit, asterisk corresponds to complex conjugation, $E_x = \tilde{E}_{0x} e^{j\delta_x} e^{j\omega t}$,
80 $E_y = \tilde{E}_{0y} e^{j\delta_y} e^{j\omega t}$ is a complex electric field of the plane wave propagating along z axis (wave vec-
81 tor $\mathbf{k} \uparrow\uparrow \mathbf{e}_z$), with $\tilde{E}_{0x}, \tilde{E}_{0y}$ being wave real amplitudes multiplied by complex $e^{-j\mathbf{k}\mathbf{r}}$ factor with
82 position \mathbf{r} , δ_x, δ_y corresponding to phases, and $E_{0x} = \tilde{E}_{0x} e^{j\delta_x}, E_{0y} = \tilde{E}_{0y} e^{j\delta_y}$ being wave complex
83 amplitudes. Both complex fields E_x, E_y can be decomposed into real (\Re) and imaginary (\Im) parts:

$$\begin{pmatrix} E_{xx} \\ E_{xy} \end{pmatrix} = \Re \begin{pmatrix} E_{0x} \\ E_{0y} \end{pmatrix}, \quad \begin{pmatrix} E_{yx} \\ E_{yy} \end{pmatrix} = \Im \begin{pmatrix} E_{0x} \\ E_{0y} \end{pmatrix}. \quad (2)$$

84 In terms of Jones formalism, it can be written as

$$|J\rangle = \begin{pmatrix} E_{0x} \\ E_{0y} \end{pmatrix} = \begin{pmatrix} E_{xx} \\ E_{yx} \end{pmatrix} + j \begin{pmatrix} E_{xy} \\ E_{yy} \end{pmatrix}. \quad (3)$$

Here, $|J\rangle$ is the non-normalized Jones vector. We emphasize that expression (3) implies that an
arbitrarily polarized electromagnetic field can be considered as a superposition of two linearly
polarized fields $\Re(|J\rangle)$ and $\Im(|J\rangle)$ containing information on the phase difference $\delta = \delta_y - \delta_x$
between them. Jones vectors for all of the pure polarization states^{42,43} can be represented in this
manner. In particular, for linear polarized light along x axis $|H\rangle$ and along y axis $|V\rangle$ we have

$$|H\rangle = \begin{pmatrix} 1 \\ 0 \end{pmatrix} = \begin{pmatrix} 1 \\ 0 \end{pmatrix} + j \begin{pmatrix} 0 \\ 0 \end{pmatrix}, \quad |V\rangle = \begin{pmatrix} 0 \\ 1 \end{pmatrix} = \begin{pmatrix} 0 \\ 1 \end{pmatrix} + j \begin{pmatrix} 0 \\ 0 \end{pmatrix}.$$

Here, $\delta_x = \delta_y = 0$. It is possible to write down both linear polarization vectors with account for
non-zero phase shifts. For example, in case $\delta_x = \delta_y = \pi/4$:

$$|H\rangle = \begin{pmatrix} 1+j \\ 0 \end{pmatrix} = \begin{pmatrix} 1 \\ 0 \end{pmatrix} + j \begin{pmatrix} 1 \\ 0 \end{pmatrix}, \quad |V\rangle = \begin{pmatrix} 0 \\ 1+j \end{pmatrix} = \begin{pmatrix} 0 \\ 1 \end{pmatrix} + j \begin{pmatrix} 0 \\ 1 \end{pmatrix}.$$

Similarly, linearly polarized light components along diagonal directions can be expressed as

$$|L_{+45^\circ}\rangle = \begin{pmatrix} 1 \\ 1 \end{pmatrix} = \begin{pmatrix} 1 \\ 1 \end{pmatrix} + j \begin{pmatrix} 0 \\ 0 \end{pmatrix}, \quad |L_{-45^\circ}\rangle = \begin{pmatrix} 1 \\ -1 \end{pmatrix} = \begin{pmatrix} 1 \\ -1 \end{pmatrix} + j \begin{pmatrix} 0 \\ 0 \end{pmatrix},$$

85 In the following, we will mostly consider Jones vectors for the right circular polarization (RCP)
86 and left circular polarization (LCP):

$$|RCP\rangle = \begin{pmatrix} 1 \\ j \end{pmatrix} = \begin{pmatrix} 1 \\ 0 \end{pmatrix} + j \begin{pmatrix} 0 \\ 1 \end{pmatrix}, \quad |LCP\rangle = \begin{pmatrix} j \\ 1 \end{pmatrix} = \begin{pmatrix} 0 \\ 1 \end{pmatrix} + j \begin{pmatrix} 1 \\ 0 \end{pmatrix}. \quad (4)$$

87 By substituting field components (2), (3) into the definition (1) and performing some straightfor-
88 ward algebra, we arrive at the following expressions for the Stokes vector:

$$\begin{pmatrix} I_p \\ Q_p \\ U_p \\ V_p \end{pmatrix} = \frac{1}{2} \begin{pmatrix} (E_{xx}^2 + E_{yx}^2) + (E_{xy}^2 + E_{yy}^2) \\ (E_{xx}^2 + E_{yx}^2) - (E_{xy}^2 + E_{yy}^2) \\ 2(E_{xx}E_{xy} + E_{yx}E_{yy}) \\ 2(E_{xx}E_{yy} - E_{yx}E_{xy}) \end{pmatrix}. \quad (5)$$

89 It is important to note that here all variables are real-valued and that \mathbf{E} components are in fact parts
90 of the real-valued linearly polarized e/m waves $\Re(|J\rangle)$, $\Im(|J\rangle)$.

91 Established relation (5) is the fundamental one to relate Stokes formalism with the existing
92 BS technique developed to trace evolution of Jones polarization vector along MC-photon trajec-
93 tories.^{13,19,47} Stokes formalism enables to immediately recognize the CPL helicity flips appearing
94 as the Stokes vector locus crossing equator on the Poincaré sphere (see Fig. 1b). We note that
95 equations (1)–(5) are written in the local reference frame of the wave.

96 2.2 Degrees of polarization

97 In order to consider partially polarized light field averaging procedures are commonly used. This
98 can clearly be seen on the example of the Wolf's coherence matrix \mathbf{J} :⁴⁸

$$\mathbf{J} = \begin{pmatrix} J_{xx} & J_{xy} \\ J_{yx} & J_{yy} \end{pmatrix} = \begin{pmatrix} \langle E_x E_x^* \rangle & \langle E_x E_y^* \rangle \\ \langle E_y E_x^* \rangle & \langle E_y E_y^* \rangle \end{pmatrix} = \frac{1}{2} \begin{pmatrix} Q + I & U + jV \\ U - jV & -Q + I \end{pmatrix}. \quad (6)$$

99 Here, $J_{xx}J_{yy} - J_{xy}J_{yx} \geq 0$. With (6) we have also provided a connection between coherence
100 matrix and Stokes parameters (I, Q, U, V) of the partially polarized light. Brackets $\langle \rangle$ correspond
101 to the field averaging procedure. Traditionally, time-averaging $\langle F(t) \rangle = \lim_{T \rightarrow \infty} \frac{1}{2T} \int_{-\infty}^{\infty} F(t) dt$ with
102 respect to the detector finite integration time T is performed, along with spectral and spatial
103 averaging defined by the resolution of the detector.^{42,48} In this work, brackets $\langle \rangle$ correspond to
104 the averaging of Monte Carlo photon intensities. This approach will be covered in the Section 3.3
105 of the paper. For partially polarized light following definitions^{43,48} for the degrees of polarization
106 based on the coherence matrix and Stokes approaches are used:

$$DoP = \sqrt{1 - \frac{4\det(\mathbf{J})}{(J_{xx} + J_{yy})^2}} = \frac{\sqrt{Q^2 + U^2 + V^2}}{I}, \quad (7)$$

107

$$DoLP = \frac{\sqrt{(J_{xx} - J_{yy})^2 + (J_{xy} + J_{yx})^2}}{J_{xx} + J_{yy}} = \frac{\sqrt{Q^2 + U^2}}{I}, \quad (8)$$

108

$$DoCP = \frac{\sqrt{2J_{yx}J_{xy} - J_{yx}^2 - J_{xy}^2}}{J_{xx} + J_{yy}} = \frac{\sqrt{V^2}}{I}. \quad (9)$$

109 Here, DoP is the total degree of polarization, $DoLP$ is the degree of linear polarization, and
 110 $DoCP$ is the degree of circular polarization, $DoP^2 = DoLP^2 + DoCP^2$. Partially polarized light
 111 can be decomposed into fully polarized and non-polarized parts:⁴³

$$\begin{pmatrix} I \\ Q \\ U \\ V \end{pmatrix} = (1 - DoP) \begin{pmatrix} I \\ 0 \\ 0 \\ 0 \end{pmatrix} + \begin{pmatrix} DoP \cdot I \\ Q \\ U \\ V \end{pmatrix}, \quad (10)$$

$$0 \leq DoP \leq 1.$$

112 Or, alternatively, partially polarized light can be treated as a superposition of two oppositely polar-
 113 ized waves:⁴³

$$\begin{pmatrix} I \\ Q \\ U \\ V \end{pmatrix} = \frac{(1 + DoP)}{2DoP} \begin{pmatrix} DoP \cdot I \\ Q \\ U \\ V \end{pmatrix} + \frac{(1 - DoP)}{2DoP} \begin{pmatrix} DoP \cdot I \\ -Q \\ -U \\ -V \end{pmatrix}, \quad (11)$$

$$0 < DoP \leq 1.$$

114 These expressions can be rewritten in more compact form by using Stokes parameters normal-
 115 ized to the intensity of the fully polarized component:

$$Q_n = \frac{Q}{DoP \cdot I}, \quad U_n = \frac{U}{DoP \cdot I}, \quad V_n = \frac{V}{DoP \cdot I}. \quad (12)$$

116 This definition allows to compute the Stokes vector values that are typically provided e.g. by
 117 ThorLabs polarimeters.⁴⁹ In addition, we can assume that $Q_n = U_n = V_n = 0$ when $DoP = 0$ (all
 118 Stokes components of the fully depolarized part are equal to zero). Then eq. (10) takes the form

$$\begin{pmatrix} I \\ Q \\ U \\ V \end{pmatrix} = (1 - DoP)I \begin{pmatrix} 1 \\ 0 \\ 0 \\ 0 \end{pmatrix} + DoP \cdot I \begin{pmatrix} 1 \\ Q_n \\ U_n \\ V_n \end{pmatrix}. \quad (13)$$

119 and (11) is written as

$$\begin{pmatrix} I \\ Q \\ U \\ V \end{pmatrix} = \frac{(1 + DoP)I}{2} \begin{pmatrix} 1 \\ Q_n \\ U_n \\ V_n \end{pmatrix} + \frac{(1 - DoP)I}{2} \begin{pmatrix} 1 \\ -Q_n \\ -U_n \\ -V_n \end{pmatrix}. \quad (14)$$

120 Now in both equations $0 \leq DoP \leq 1$.

121 Important specific cases of the expressions (13), (14) include decomposition of the circularly
 122 polarized light into the fully polarized right- and left-handed parts and decomposition of the lin-
 123 early polarized light into orthogonal components. For the first case, we rewrite (13) as

$$\begin{pmatrix} I \\ 0 \\ 0 \\ V \end{pmatrix} = (1 - DoCP)I \left(\frac{1}{2} \begin{pmatrix} 1 \\ 0 \\ 0 \\ -1 \end{pmatrix} + \frac{1}{2} \begin{pmatrix} 1 \\ 0 \\ 0 \\ 1 \end{pmatrix} \right) + DoCP \cdot I \begin{pmatrix} 1 \\ 0 \\ 0 \\ 1 \end{pmatrix},$$

124 after terms regroup arriving at

$$\begin{pmatrix} I \\ 0 \\ 0 \\ V \end{pmatrix} = \frac{(1 - DoCP)I}{2} \begin{pmatrix} 1 \\ 0 \\ 0 \\ -1 \end{pmatrix} + \frac{(1 + DoCP)I}{2} \begin{pmatrix} 1 \\ 0 \\ 0 \\ 1 \end{pmatrix}, \quad (15)$$

This alternative form of the expression (14) allows to write down expressions for the co- and cross-polarized light components via $DoCP$:

$$I_R = \frac{1}{2}(1 + DoCP)S_0, \quad I_L = \frac{1}{2}(1 - DoCP)S_0.$$

125 Here, I_R corresponds to the RCP light and I_L corresponds to the LCP light. $DoCP$ value can then
 126 be estimated as

$$DoCP = \frac{I_R - I_L}{I_R + I_L}. \quad (16)$$

127 We note that this expression has to be treated with care: when $I_L > I_R$, we supposedly arrive
 128 at negative $DoCP$ values. However, this does not actually contradict the definition (9), because
 129 expression (16) is derived under the assumption that RCP intensity is always larger than LCP
 130 one, as follows from (15). Otherwise, we should appropriately rewrite these equations, arriving at
 131 $DoCP = (I_L - I_R) / (I_L + I_R)$, which generally results in $DoCP = |I_R - I_L| / (I_R + I_L)$ fully
 132 complying with (9).

133 Similar decomposition can be written for the second case when light is linearly polarized:

$$\begin{pmatrix} I \\ Q \\ U \\ 0 \end{pmatrix} = \frac{(1 + DoLP)I}{2} \begin{pmatrix} 1 \\ Q_n \\ U_n \\ 0 \end{pmatrix} + \frac{(1 - DoLP)I}{2} \begin{pmatrix} 1 \\ -Q_n \\ -U_n \\ 0 \end{pmatrix}, \quad (17)$$

134 which in turn reduces to

$$\begin{pmatrix} I \\ Q \\ 0 \\ 0 \end{pmatrix} = \frac{(1 + DR)I}{2} \begin{pmatrix} 1 \\ 1 \\ 0 \\ 0 \end{pmatrix} + \frac{(1 - DR)I}{2} \begin{pmatrix} 1 \\ -1 \\ 0 \\ 0 \end{pmatrix} \quad (18)$$

135 when $U = 0$. Here, $DR = |Q|/I$ and all polarization degrees are within $[0, 1]$ limits. Inten-
 136 sities of horizontally $I_{||}$ and vertically I_{\perp} polarized light can be obtained from (18) to express

137 $DR = \frac{I_{\parallel} - I_{\perp}}{I_{\parallel} + I_{\perp}}$. This expression for DR has been used throughout most of the previous works.¹³
 138 Degree of total linear polarization $DoLP$ also involves intensities of light linearly polarized along
 139 $+45^{\circ}, -45^{\circ}$ axes:⁴³

$$DoLP = \frac{\sqrt{(I_{\parallel} - I_{\perp})^2 + (I_{+45^{\circ}} - I_{-45^{\circ}})^2}}{I}. \quad (19)$$

140 Here, $I = I_{\parallel} + I_{\perp} = I_{+45^{\circ}} + I_{-45^{\circ}} = I_R + I_L$. Now, we have established theoretical background
 141 and can proceed with the description of the developed MC approach.

142 3 Monte Carlo based on the Bethe-Salpeter equation

143 3.1 Tracking of the Jones polarization vector

144 Within the BS-based Monte Carlo model,^{13,19,33} a large amount ($N_{inc} > 10^9$) of MC-photons with
 145 pre-defined statistical weight $W_j, j = [1 \dots N_{inc}]$ is launched from the source oriented under θ_i angle
 146 to the surface normal, propagates through the turbid medium and statistics is collected from those
 147 $N_{ph} < N_{inc}$ arrived on the detector oriented under $-\theta_d$ angle to the surface normal (see Fig. 2).
 148 Here, the minus sign corresponds to the opposite direction of the detector to the surface normal as
 149 compared with the direction of the source. Turbid medium is defined by scattering coefficient μ_s ,

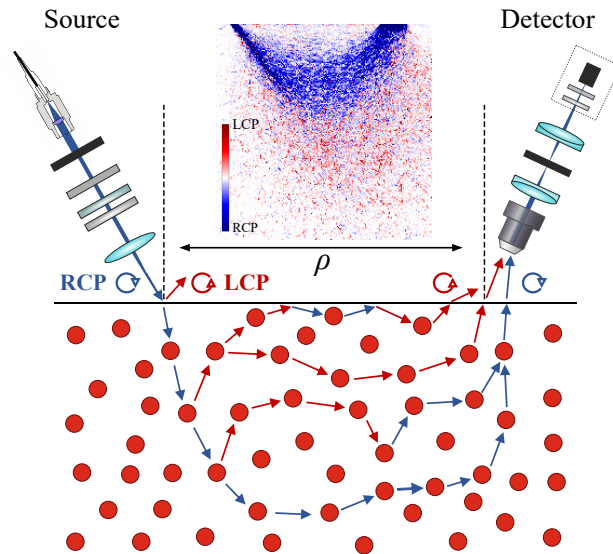


Fig 2 Illustration of the backscattering model with schematically depicted elements of the experimental setup.⁴⁻⁶ Sample with known optical properties is illuminated with RCP light. Possible MC-photon trajectories with zero, one and two backscattering events and with photon-surface interactions are presented. Each backscattering event causes a helicity flip represented by the color of the direction arrow. The experimental configuration involves supercontinuum fiber laser source filtered by the acousto-optic tunable filter. The resulting RCP is produced with the half-wave and quarter-wave plates and is focused on the medium surface under θ_i angle. The detector is oriented under $-\theta_d$ angle to the surface normal, collects backscattered light with $20\times$ objective lens and measures Stokes parameters of the registered light with a polarimeter.⁴⁹ The inset shows simulated sampling volumes for RCP and LCP light components at the relatively large source-detector separation distance ρ (see Sec. 4.3 for more details).

150 absorption coefficient μ_a , anisotropy parameter g and refractive index n .¹⁸ Additionally, tissue-
 151 like medium implies low contrast between refractive indices of the host medium and scatterers
 152 (e.g. cellular components, organelles, extracellular matrices and other microstructures).

153 In this work we consider a uniform distribution of MC-photons, noting that in general our
 154 approach allows to simulate spatial and phase distributions for a wide variety of light beams, in-
 155 cluding Gaussian, Bessel, Hermite-Gaussian and Laguerre-Gaussian beams with complex shape
 156 carrying orbital angular momentum (OAM). To account for these beam types it is necessary both
 157 to ensure the appropriate initial distribution of the MC-photons relevant to the beam intensity and
 158 phase profiles and to set the correct initial directions of the MC-photons according to the Poynting
 159 vector trajectories that render energy transfer within the beam.^{50,51} With the next development, we
 160 plan to implement this technique in our model to investigate the conservation of OAM in tissue-like
 161 medium.

162 Each MC-photon at the source is characterized by the initial statistical weight W_{0j} , Cartesian
 163 coordinates $(x_0, y_0, 0)$, propagation direction \mathbf{s}_0 (defined both by beam structure and angle θ_i be-
 164 tween source and surface normal, see Fig. 2) and, most importantly, by the initial polarization state.
 165 We introduce a real-valued vector \mathbf{P} that corresponds to the direction of the linearly polarized \mathbf{E}
 166 field.^{13,19,32-34,39} By assigning a pair of these vectors $\mathbf{P}_x = (P_{xx}, P_{xy}, P_{xz})$, $\mathbf{P}_y = (P_{yx}, P_{yy}, P_{yz})$
 167 to each MC-photon we are able to define two separate independent linear polarization states sim-
 168 ilarly to (3). It is important to note that here both polarization vectors are written in the global
 169 Cartesian coordinate system (x, y, z) and that they are orthogonal to the MC-photon unit prop-
 170 agation direction. If photon direction coincides with the z axis, then sum of $\mathbf{P}_x \sim \Re(|J\rangle)$ and
 171 $\mathbf{P}_y \sim \Im(|J\rangle)$ can be interpreted as Jones vector: $|J\rangle = \mathbf{P}_x + j\mathbf{P}_y$. We emphasize that from \mathbf{P}_x
 172 and \mathbf{P}_y we can always compute the Jones vector associated with the MC-photon and vice versa:
 173 by knowing the polarization state (Jones vector) of the MC-photon we can always reconstruct \mathbf{P}_x
 174 and \mathbf{P}_y values.

After launch, all MC-photons undergo surface ($z = 0$) interaction and are transmitted to the
 turbid medium layer with account for the Snell's law and the appropriate Fresnel coefficients influ-
 encing MC-photon weights, directions and polarization (see Sec. 3.2). In turbid medium ($z > 0$)
 each MC-photon trajectory is modeled as a sequence of the elementary simulations containing lim-
 ited amount of scattering events N_{scatt} . This procedure has been thoroughly covered in the previous
 works.^{13,19,47} At each i 'th scattering event, $i = [1 \dots N_{scatt}]$, the following computational steps are
 performed: random path length $l_i = -\ln\xi/\mu_s$ is computed (in this paper, we assume that $\mu_a \ll \mu_s$
 and $\xi \in (0, 1]$ is a uniformly distributed random number), MC-photon is moved to the next position
 $\mathbf{r}_i = \mathbf{r}_{i-1} + \mathbf{s}_i l_i$ with weight attenuated according to the Beer-Lambert law ($W_i = W_{i-1} e^{-\mu_a l_i}$),
 and the next propagation direction \mathbf{s}_{i+1} is evaluated via inversion of the Henyey-Greenstein (HG)
 phase function⁵²

$$p_{HG}(\cos \theta') = \frac{1}{4\pi} \frac{1 - g^2}{(1 + g^2 - 2g \cos \theta')^{3/2}},$$

175 where θ' is the polar scattering angle in the MC-photon reference plane. Here, we have used the po-
 176 sition vector $\mathbf{r}_i = (x_i, y_i, z_i)$ and the unit direction for the each scattering event $\mathbf{s}_i = [s_X, s_Y, s_Z]_i =$
 177 $[\sin \theta \cos \varphi, \sin \theta \sin \varphi, \cos \theta]_i$, with θ, φ as azimuthal and polar angles that correspond to the global
 178 Cartesian coordinates. HG function has been traditionally employed in the MC simulations as a
 179 substitute to the rigorous Mie phase function due to its high performance and the ability to provide
 180 realistic results complying with the experimental tissue measurements^{15,53,54}. It should be noted

181 that, basically, any phase function p can be used.^{55,56} If analytical inversion of p is not possible, e.g.
 182 for the case of Mie scattering, then table lookup method is involved to ensure fast computational
 183 speed.

184 At each step we check if MC-photon path crosses the medium boundary and invoke surface
 185 refraction-transmission and detection procedures if this is the case (see Sec. 3.2). Evolution of each
 186 linearly polarized state $\mathbf{P}_x, \mathbf{P}_y$ can be traced along the MC-photon trajectory $\mathbf{r}_i, i = [1 \dots N_{scatt}]$ via
 187 the following procedure which is obtained from the iterative solution to BS equation:^{13,14,19}

$$\mathbf{P}_i = -\mathbf{s}_i \times [\mathbf{s}_i \times \mathbf{P}_{i-1}] = \underbrace{\left[\hat{I} - \mathbf{s}_i \otimes \mathbf{s}_i \right]}_{\hat{\mathbf{U}}_i} \mathbf{P}_{i-1}, \quad (20)$$

Here, \hat{I} is the third-rank unit tensor and \otimes indicates the direct product. Tensor $\left[\hat{I} - \mathbf{s}_i \otimes \mathbf{s}_i \right]$ can
 be explicitly rewritten in the form of 3x3 real operator $\hat{\mathbf{U}}_i$:³²

$$\hat{\mathbf{U}}_i = \begin{pmatrix} 1 - s_{iX}^2 & -s_{iX} \cdot s_{iY} & -s_{iX} \cdot s_{iZ} \\ -s_{iX} \cdot s_{iY} & 1 - s_{iY}^2 & -s_{iY} \cdot s_{iZ} \\ -s_{iX} \cdot s_{iZ} & -s_{iX} \cdot s_{iZ} & 1 - s_{iZ}^2 \end{pmatrix}.$$

188 Most importantly, operator $\hat{\mathbf{U}}_i$ guarantees that the electromagnetic field remains transversal ex-
 189 periencing the i -th scattering event. It can be applied to both linear polarization vectors $\mathbf{P}_x, \mathbf{P}_y$
 190 simultaneously as follows from (2), and it accounts for the helicity flips when considering pair
 191 of the polarization vectors that correspond to the circularly or elliptically polarized MC-photon
 192 (see Fig. 1a). Eventually, the chain $\hat{\mathbf{U}}_N \hat{\mathbf{U}}_{N-1} \hat{\mathbf{U}}_{N-2} \dots \hat{\mathbf{U}}_2 \hat{\mathbf{U}}_1$ of projection operators transforms the
 193 initial polarization \mathbf{P}_{x_0} upon a sequence of N scattering events to the final polarization \mathbf{P}_{x_N} :¹⁹

$$\mathbf{P}_{x_N} = \hat{\mathbf{U}}_N \hat{\mathbf{U}}_{N-1} \hat{\mathbf{U}}_{N-2} \dots \hat{\mathbf{U}}_1 \mathbf{P}_{x_0}. \quad (21)$$

194 The same expression can be used to relate \mathbf{P}_{y_N} and \mathbf{P}_{y_0} as follows from eq. (2). It is important to
 195 note that this procedure always ensures \mathbf{P}_{x_i} and \mathbf{P}_{y_i} to be orthogonal to the MC-photon direction
 196 \mathbf{s}_i at each scattering event. It means that if we rewrite \mathbf{P}_{x_i} and \mathbf{P}_{y_i} in terms of the MC-photon
 197 local reference frame using the appropriate transformation matrix, we will obtain Jones vectors
 198 with third component equal to zero. This peculiarity can be verified e.g. numerically, but, most
 199 importantly, polarization tracing (21) does not inherently require reference frame tracking and
 200 allows to avoid computation of the scattering and rotation matrices as proposed by the VRTE-
 201 based approaches,^{23,28} leading to the computational demand of polarization-enabled MC to be
 202 comparable to the demand of scalar MC. Tensor $\hat{\mathbf{U}}_i$ ensures that each individual MC-photon always
 203 remains fully polarized. Then Stokes vector values can be obtained for each MC-photon at any
 204 scattering event via equation (5) with \mathbf{E} values replaced by the corresponding $\mathbf{P}_{x_i}, \mathbf{P}_{y_i}$ components.

205 We should explicitly note that the approach based on the Bethe-Salpeter equation was rigor-
 206 ously introduced for the case of pure Rayleigh scattering.³² In case of biotissues we, however, deal
 207 with scatterers with the size comparable to or a few times higher than the wavelength λ . Keeping
 208 in mind that within biological media fluctuation of the relative refractive index n_r between the
 209 scatterer (e.g. cell component such as nucleus, n_s) and the surrounding medium (e.g. cytoplasm,
 210 n_m) is typically small ($|n_r - 1| < 0.1, n_r = n_s/n_m$),¹⁸ we conclude that we actually deal with

211 the so-called soft scattering particles.^{57,58} In this case, particle size d should obey the relation
 212 $kd|n_r - 1| \ll 1$, where $k = 2\pi/\lambda$. Then Rayleigh-Gans-Debye (RGD) approach can be applied
 213 to describe scattering by soft particles characterized by the non-isotropic scattering phase func-
 214 tion.^{32,57,58} On these grounds, the proposed BS-based Monte Carlo polarization tracing can be
 215 treated as the first-order approximation to RGD and applied to simulate polarized light scattering
 216 in biological media.^{19,32} We also note that in this paper non-birefringent and non-optically active
 217 medium is considered: while birefringence is known to be an important feature of biological tis-
 218 sues, it has been reported that e.g. for skin it is almost impossible to observe the phase changes
 219 occurring due to birefringence at normal conditions.⁵⁹ At the same time, account for birefringence
 220 can be added into the developed model by properly implementing account for the ordinary and
 221 extraordinary optical pathlengths of MC-photons influencing the phase shift and polarization state.

222 We repeat the outlined computational steps for each scattering event until one of the follow-
 223 ing conditions is met: either $W_i < 10^{-4}$ (statistical weight becomes negligible as follows from
 224 the Beer-Lambert law) or the amount of scattering events N_{scatt} becomes larger than 10^3 . These
 225 limitations ensure proper trajectory tracing cut-off.¹⁹ We continue launching MC-photons until the
 226 certain amount (no less than $N_{ph} = 10^5$) arrives on the detector. Detection procedure consists of
 227 the two checks: MC-photon coordinates should lie within the detector area ($-r_d + \rho \leq x_N \leq$
 228 $r_d + \rho, -r_d \leq y_N \leq r_d, z_N = 0$), and refracted direction \mathbf{s}_N should meet the detector numerical
 229 aperture (NA) requirements. We would limit those directions by using $\text{acos}(\mathbf{s}_N \cdot \mathbf{s}_d) < NA$, where
 230 $\mathbf{s}_d = [\sin(-\theta_d), 0, \cos(-\theta_d)]$ is the unit vector collinear to the detector axis. Both here and in the
 231 subsequent sections N is considered to be an index of the detection event.

232 3.2 Interface influence

233 Operator \hat{U}_i allows us to trace the polarization evolution at each scattering event within the turbid
 234 medium, as shown by eq. (21). However, it does not account for the phenomena occurring at the
 235 medium boundaries. In this case, the well-known Fresnel coefficients have to be applied to polar-
 236 ized light:⁴⁸ $T_P = \frac{2n_1 \cos \theta_c}{n_2 \cos \theta_c + n_1 \cos \theta_t}$, $T_S = \frac{2n_1 \cos \theta_c}{n_1 \cos \theta_c + n_2 \cos \theta_t}$, $R_P = \frac{n_2 \cos \theta_c - n_1 \cos \theta_c}{n_2 \cos \theta_c + n_1 \cos \theta_t}$,
 237 $R_S = \frac{n_1 \cos \theta_c - n_2 \cos \theta_t}{n_1 \cos \theta_c + n_2 \cos \theta_t}$. Here, T_P, T_S correspond to the transmission coefficients for P- and
 238 S-polarized (or $|H\rangle$ and $|V\rangle$) waves, and R_P, R_S correspond to the reflection coefficients. We have
 239 also introduced angle of the incident light θ_c , angle of the transmitted light θ_t , and medium refrac-
 240 tive indices $n_{1,2}$. Fresnel coefficients can be complex-valued, for example, in case of total internal
 241 reflection due to Snell law $n_1 \sin \theta_c = n_2 \sin \theta_t$. As a consequence, these coefficients can not be
 242 separately applied to each linear polarization vector $\mathbf{P}_{x,y}$; instead, the complex counterpart of (3)
 243 has to be reconstructed from the pair of vectors (2) prior to applying Fresnel coefficients. After
 244 that, the new reflected or transmitted vectors can be decomposed back into two separate linear
 245 polarization states, and polarization tracing procedure from Sec. 3.1 can be continued. We also
 246 have to keep in mind that Fresnel coefficients are derived in the wave's plane of incidence.⁴⁸ It
 247 means that at the event of the MC-photon interaction with the surface we have to rewrite both \mathbf{P}
 248 vectors in the corresponding reference frame (x', y', z') , defined by the MC-photon direction and
 249 its projection to the interface of the surface, via applying proper transformation matrix.

250 If $i - 1$ is the index of the event of the MC-photon interaction with the surface, and i is the index
 251 of the next scattering event, account for the Fresnel coefficients can be mathematically expressed
 252 in the following form: $(P'_x)_i = (P'_x)_{i-1} \cdot R_P$, $(P'_y)_i = (P'_y)_{i-1} \cdot R_S$, $(P'_z)_i = (P'_z)_{i-1} \cdot R_P$. Here, \mathbf{P}'

253 are polarization vectors transformed to the reference frame associated with the MC-photon's plane
 254 of incidence. In terms of polarization vector components:

$$\begin{aligned}
 (P'_{xx})_i &= \Re(R_P)(P'_{xx})_{i-1} - \Im(R_P)(P'_{yx})_{i-1}, & (P'_{yx})_i &= \Im(R_P)(P'_{xx})_{i-1} + \Re(R_P)(P'_{yx})_{i-1}, \\
 (P'_{xy})_i &= \Re(R_S)(P'_{xy})_{i-1} - \Im(R_S)(P'_{yy})_{i-1}, & (P'_{yy})_i &= \Im(R_S)(P'_{xy})_{i-1} + \Re(R_S)(P'_{yy})_{i-1}, \\
 (P'_{xz})_i &= \Re(R_P)(P'_{xz})_{i-1} - \Im(R_P)(P'_{yz})_{i-1}, & (P'_{yz})_i &= \Im(R_P)(P'_{xz})_{i-1} + \Re(R_P)(P'_{yz})_{i-1}.
 \end{aligned}
 \tag{22}$$

255 For the transmission it is enough to replace R_P, R_S with their counterparts T_P, T_S . At the same
 256 time, in the specific case of linearly polarized light where phase information is not usually relevant
 257 the field has only one polarization vector \mathbf{P}_x , and it is possible to account for polarization changes
 258 at the interface via absolute values $|T_P|^2, |T_S|^2, |R_P|^2, |R_S|^2$ of Fresnel coefficients as outlined in
 259 the previous works.¹³ This procedure influences the absolute value of polarization vectors, and,
 260 correspondingly, the weight of each MC-photon. After account for the interface influence, both
 261 \mathbf{P}' vectors are transformed back to the global (x, y, z) reference frame. We would further use the
 262 notations (x', y', z') and \mathbf{P}' in order to emphasize that non-laboratory reference frame is used: in
 263 addition to the plane of incidence, this could be either source or detector reference frame, or local
 264 reference frame of the MC-photon.

265 We also note that it is necessary to properly select transmitted or reflected MC-photons in
 266 multilayered medium. It can be done via implementing selection procedure following Wang¹⁵
 267 at each interface between medium layers, adding proper account for the polarization state of the
 268 MC-photon. In this work we consider homogeneous scattering medium with single layer.

269 3.3 Detected light intensity components, Stokes vector and polarization degrees

270 Each MC-photon that arrived on the detector is fully polarized and its polarization state is known
 271 from (21) with account for reflections/refractions by (22). Every detected MC-photon also pos-
 272 sesses weight attenuated with respect to the Beer–Lambert law $W_{N_j} = W_{0_j} \exp\left(-\mu_a \sum_{i=1}^{N_j} l_i\right)$,
 273 where $0 < N_j < N_{scatt}$ is index of the detection event for j 'th MC-photon and l_i is the path length
 274 between two neighbouring scattering events. If detector plane is parallel to the medium surface,
 275 then averaging of the MC-photon ensemble intensity components is performed as follows:^{34,39}

$$I_R = \frac{1}{4N_{inc}} \sum_{j=1}^{N_{ph}} W_{N_j} (P_{xx}^2 + P_{yx}^2 + P_{xy}^2 + P_{yy}^2 + 2P_{xx}P_{yy} - 2P_{yx}P_{xy})_{N_j} \Gamma_R^{N_j}, \tag{23}$$

$$I_L = \frac{1}{4N_{inc}} \sum_{j=1}^{N_{ph}} W_{N_j} (P_{xx}^2 + P_{yx}^2 + P_{xy}^2 + P_{yy}^2 - 2P_{xx}P_{yy} + 2P_{yx}P_{xy})_{N_j} \Gamma_R^{N_j}, \tag{24}$$

277 For completeness, we also provide expressions for all intensities of the linearly polarized light:

$$I_{+45^\circ} = \frac{1}{4N_{inc}} \sum_{j=1}^{N_{ph}} W_{N_j} (P_{xx}^2 + P_{yx}^2 + P_{xy}^2 + P_{yy}^2 + 2P_{xx}P_{xy} + 2P_{yx}P_{yy})_{N_j} \Gamma_R^{N_j}, \tag{25}$$

$$I_{-45^\circ} = \frac{1}{4N_{inc}} \sum_{j=1}^{N_{ph}} W_{N_j} (P_{xx}^2 + P_{yx}^2 + P_{xy}^2 + P_{yy}^2 - 2P_{xx}P_{xy} - 2P_{yx}P_{yy})_{N_j} \Gamma_R^{N_j}, \tag{26}$$

279

$$I_{\parallel} = \frac{1}{2N_{inc}} \sum_{j=1}^{N_{ph}} W_{N_j} (P_{xx}^2 + P_{yx}^2)_{N_j} \Gamma_R^{N_j}, \quad (27)$$

280

$$I_{\perp} = \frac{1}{2N_{inc}} \sum_{j=1}^{N_{ph}} W_{N_j} (P_{xy}^2 + P_{yy}^2)_{N_j} \Gamma_R^{N_j}. \quad (28)$$

281 Here, $\Gamma_R = \frac{2}{1 + \cos^2 \theta}$ is the Rayleigh factor derived from the optical theorem in Born approx-
 282 imation and $\cos^2 \theta$ is the square cosine of the scattering angle weighted by the single scattering
 283 cross-section.^{13,19,32,33} For an arbitrary orientation of the detector (see Fig. 2) both \mathbf{P}_x and \mathbf{P}_y are
 284 supposed to be rewritten in the new Cartesian basis with z' axis being collinear to the detector axis.

285 Stokes parameters are related to the light intensity components as:

$$Q = I_{\parallel} - I_{\perp}, \quad U = I_{+45^\circ} - I_{-45^\circ}, \quad V = I_R - I_L, \quad (29)$$

286

Final expressions for the Stokes parameters withing the BS-based MC are:

$$I = \frac{1}{2N_{inc}} \sum_{j=1}^{N_{ph}} W_{N_j} (P_{xx}^2 + P_{yx}^2 + P_{xy}^2 + P_{yy}^2)_{N_j} \Gamma_R^{N_j}, \quad (30a)$$

287

$$Q = \frac{1}{2N_{inc}} \sum_{j=1}^{N_{ph}} W_{N_j} (P_{xx}^2 + P_{yx}^2 - P_{xy}^2 - P_{yy}^2)_{N_j} \Gamma_R^{N_j}, \quad (30b)$$

288

$$U = \frac{1}{N_{inc}} \sum_{j=1}^{N_{ph}} W_{N_j} (P_{xx}P_{xy} + P_{yx}P_{yy})_{N_j} \Gamma_R^{N_j}, \quad (30c)$$

289

$$V = \frac{1}{N_{inc}} \sum_{j=1}^{N_{ph}} W_{N_j} (P_{xx}P_{yy} - P_{yx}P_{xy})_{N_j} \Gamma_R^{N_j}. \quad (30d)$$

290 Degrees of polarization can then be computed either via definitions (7)–(9) or, equivalently,
 291 via expressions for intensity components (16), (19). Depending on the detection conditions, it
 292 might be necessary to compute any of the given parameters in the reference frame other than the
 293 global one, e.g. in the detector reference frame or in the local reference frame of each MC-photon.
 294 For this purpose transformation matrix providing \mathbf{P}' in the selected reference frame (x', y', z') can
 295 be used. The obtained \mathbf{P}' values can be directly substituted into (23)–(30) providing appropriate
 296 intensity, Stokes or degree of polarization values.

297 3.4 Computation of Mueller matrix components

We have demonstrated that within the proposed MC approach such parameters as Jones vector (21), Stokes vector for partially polarized light (30), Wolf coherence matrix (6) and degrees of

polarization (7–9) can be evaluated. We also stress that it is possible to compute Mueller matrix elements. We consider Mueller matrix in its general form:

$$M = \begin{bmatrix} m_{11} & m_{12} & m_{13} & m_{14} \\ m_{21} & m_{22} & m_{23} & m_{24} \\ m_{31} & m_{32} & m_{33} & m_{34} \\ m_{41} & m_{42} & m_{43} & m_{44} \end{bmatrix}, \quad \begin{pmatrix} I \\ Q \\ U \\ V \end{pmatrix}_{out} = M \begin{pmatrix} I \\ Q \\ U \\ V \end{pmatrix}_{in}.$$

298 Mueller matrix elements are usually measured with the following setup configurations⁶⁰

$$M = \begin{bmatrix} OO & HO - VO & PO - MO & LO - RO \\ OH - OV & (HH + VV) - (HV + VH) & (PH + MV) - (PV + MH) & (LH + RV) - (LV + RH) \\ OP - OM & (HP + VM) - (HM + VP) & (PP + MM) - (PM + MP) & (LP + RM) - (LM + RP) \\ OL - OR & (HL + VR) - (HR + VL) & (PL + MR) - (PR + ML) & (LL + RR) - (RL + LR) \end{bmatrix}. \quad (31)$$

299 Here, the first letter corresponds to the source polarization, and the second letter corresponds to
300 the measured intensity (with analyzer): O – non-polarized light, H corresponds to I_{\parallel} , V – to I_{\perp} ,
301 P – to $I_{+45^{\circ}}$, M – to $I_{-45^{\circ}}$, R – to I_R and L – to I_L . In terms of our model, Mueller matrix \mathcal{M} of
302 the single detected photon can be expressed as:

$$\begin{aligned} \mathcal{M}_{11} &= I & \mathcal{M}_{12} &= P_{xx}^2 + P_{xy}^2 - P_{yx}^2 - P_{yy}^2 & \mathcal{M}_{13} &= \mathcal{P}_{xx}^2 + \mathcal{P}_{xy}^2 - \mathcal{P}_{yx}^2 - \mathcal{P}_{yy}^2 & \mathcal{M}_{14} &= 0 \\ \mathcal{M}_{21} &= \mathcal{M}_{12} & \mathcal{M}_{22} &= P_{xx}^2 - P_{xy}^2 - P_{yx}^2 + P_{yy}^2 & \mathcal{M}_{23} &= \mathcal{P}_{xx}^2 - \mathcal{P}_{xy}^2 - \mathcal{P}_{yx}^2 + \mathcal{P}_{yy}^2 & \mathcal{M}_{24} &= 0 \\ \mathcal{M}_{31} &= \mathcal{M}_{12}^{rot} & \mathcal{M}_{32} &= P_{xx}P_{xy} - P_{yx}P_{yy} & \mathcal{M}_{33} &= \mathcal{P}_{xx}\mathcal{P}_{xy} - \mathcal{P}_{yx}\mathcal{P}_{yy} & \mathcal{M}_{34} &= 0 \\ \mathcal{M}_{41} &= \mathcal{M}_{14} & \mathcal{M}_{42} &= 0 & \mathcal{M}_{43} &= 0 & \mathcal{M}_{44} &= P_{xx}P_{yy} - P_{xy}P_{yx} \end{aligned} \quad (32)$$

303 Here, $P_x = (P_{xx}, P_{xy}, P_{xz})$ and $P_y = (P_{yx}, P_{yy}, P_{yz})$ are the real-valued vectors introduced in
304 Sec. 3.1 and computed via eq. (21) for incident linear polarizations $|H\rangle = P_{x_0} = (1, 0, 0)$,
305 $|V\rangle = P_{y_0} = (0, 1, 0)$. Similarly, $\mathcal{P}_x = (\mathcal{P}_{xx}, \mathcal{P}_{xy}, \mathcal{P}_{xz})$ and $\mathcal{P}_y = (\mathcal{P}_{yx}, \mathcal{P}_{yy}, \mathcal{P}_{yz})$ are vectors
306 computed for incident diagonal linear polarizations $|L_{+45^{\circ}}\rangle = \mathcal{P}_{x_0} = (\frac{\sqrt{2}}{2}, \frac{\sqrt{2}}{2}, 0)$, $|L_{-45^{\circ}}\rangle =$
307 $\mathcal{P}_{y_0} = (\frac{\sqrt{2}}{2}, -\frac{\sqrt{2}}{2}, 0)$. Circular polarization states $|RCP\rangle$ and $|LCP\rangle$ are accounted for as su-
308 perpositions of $|H\rangle$ and $|V\rangle$ according to eq. (4). $\mathcal{M}_{31} = \mathcal{M}_{12}^{rot}$ means that this element can be
309 obtained via rotation of \mathcal{M}_{12} by $-\pi/4$.⁶⁰ Matrix (32) is valid when the detector plane coincides
310 with the medium surface, as outlined in Sec. 3.3. Mueller matrix of the detected signal can then
311 be obtained via the ensemble averaging procedure following the (23)–(28):

$$M = \sum_{j=1}^{N_{ph}} W_{N_j} \mathcal{M}_{N_j} \Gamma_R^{N_j}. \quad (33)$$

312 Here, \mathcal{M}_{N_j} corresponds to the Mueller matrix of the j -th photon which was detected at the N_j
313 scattering event, and all Mueller matrix elements are independently multiplied by the scalar term
314 $W_{N_j} \Gamma_R^{N_j}$ for each photon. Now our formulation of the generalized BS-based polarization Monte
315 Carlo is complete. We emphasize that with (32)–(33) we can compute Mueller matrix within
316 one simulation, so it is not required to launch separate MC-photons with different polarization
317 states. This factor, along with the remarks made in Sec. 3.1 (see (21)), contributes to the high
318 computational performance of our approach.

4 Results and discussion

4.1 Setup configuration

Our theoretical model is oriented towards the most common experimental setups employed to study both forward (transmission) scattering and backscattering by biotissues with non-invasive diagnostic purposes.⁶¹ In particular, we verify the obtained simulation results against measurements performed with the backscattering setup which has been thoroughly described in our previous works.⁴⁻⁶ In this setup we employ multiwavelength 450–650 nm light source with 15 μm diameter incident under θ_i on the tissue-like surface characterized by μ_s, μ_a, g and n . In the following, these values are selected to closely match the properties of real tissues or tissue phantoms.⁶² Incident light is right circularly polarized. We collect the scattered depolarized signal in the detector with 50 μm diameter oriented under θ_d with respect to surface normal and separated from the source by distance ρ (see Fig. 2). In order to properly study the evolution of CPL, we use an infinity-corrected objective in the detection arm ensuring that polarimeter registers Stokes parameters that correspond to the MC-photon local reference frames.

In the current paper, incident $|RCP\rangle$ beam is simulated as a plane wave (uniform distribution of MC-photons, direction defined solely by θ_i) with $\lambda = 640 \text{ nm}$ and polarization vectors defined as $\mathbf{P}'_{x_0} = (1, 0, 0)$, $\mathbf{P}'_{y_0} = (0, 1, 0)$ in the reference frame of the source. In the global reference frame which is further employed in the scattering simulation these vectors take the following form: $\mathbf{P}_{x_0} = (\cos \theta_i, 0, \sin \theta_i)$, $\mathbf{P}_{y_0} = (0, 1, 0)$. In the model, we consider two source-detector configurations: with the angular incidence and collection of light ($\theta_i = 55^\circ, \theta_d = 30^\circ$), and with the vertically positioned source and detector ($\theta_i = \theta_d = 0$). The ρ value is scaled to the transport mean free path $l^* = \mu_s^{-1}(1 - g)^{-1}$ representing the average distance that light propagates before its direction of propagation is randomized.^{58,63,64} We collect detector statistics (23)–(30) via evaluating polarization vectors in the local reference frame for each MC-photon, which corresponds to the experimental detection conditions.

4.2 Depolarization of the CPL backscattered by turbid tissue-like medium

We investigate the process of CPL depolarization in terms of the Stokes vector and light intensity components both via processing surface signal registered by the detector (see Sec. 3.1) and via analyzing in-depth distribution of the detected response represented by sampling volume.^{16,17} Main results are summarized in Figure 3. We begin the analysis by studying the intensity components of the scattered light. Figures 3b and 3c show an interplay of the oppositely polarized *RCP* (blue) and *LCP* (red) intensities upon increase of the source-detector separation ρ/l^* . As one can see, for the short separation distances ($\rho/l^* < 1$ for the vertical setup and $\rho/l^* < 0.8$ for the angular setup), the helicity of incident *RCP* light is flipped due to backscattering, and the flipped *LCP* light is inversely related to the emerging *RCP* component. The *LCP* light is formed due to odd number of the helicity flips occurred along the consecutive scattering events within the medium between points of incidence and detection, whereas appearance of *RCP* is based on the even number of flips.⁴⁴ The decrease of *LCP* with the increase of source-detector separation is compensated with the proportional increase of *RCP* light, clearly illustrating predictions (15).

The *RCP* stream becomes dominating over the *LCP* at larger source-detector separation ($\rho > l^*$). This allows us to conclude that the angular momentum of light is preserved, and that multiple scattering maintains the helicity of incident circularly polarized light (*RCP*). At the flip

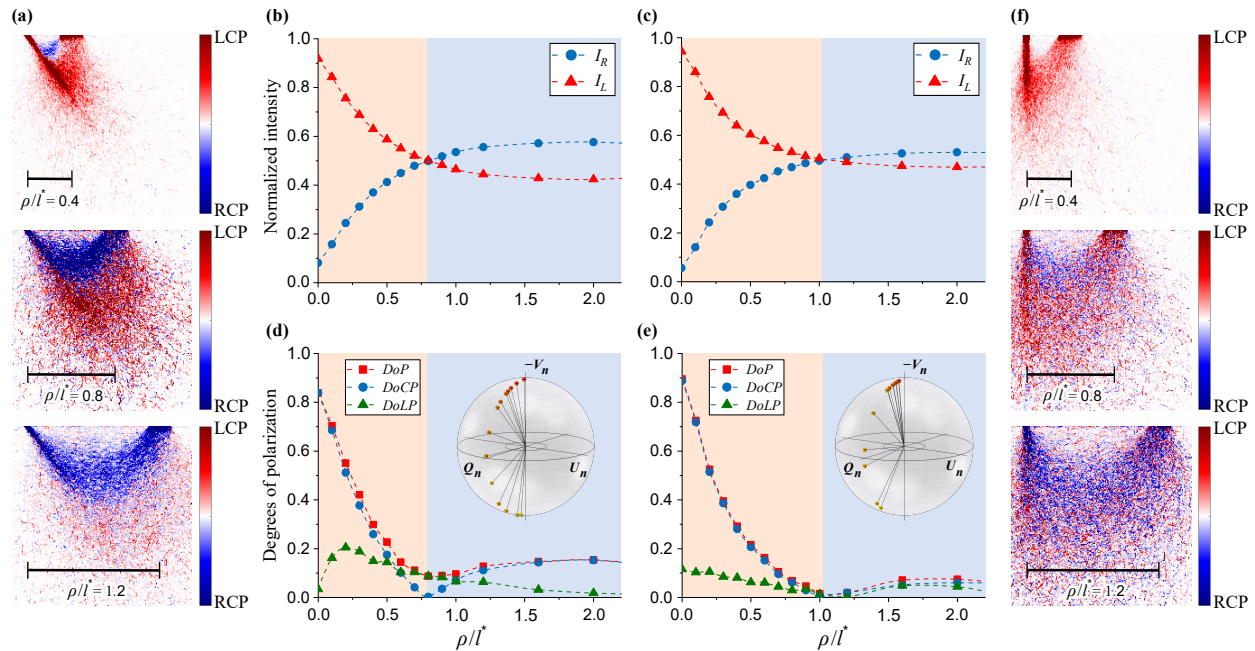


Fig 3 (a) Difference between sampling volumes for the intensity of cross-polarized I_L (red) and co-polarized I_R (blue) light arriving on the detector for the $\theta_i = 55^\circ, \theta_d = 30^\circ$ setup configuration with the variable source-detector separation distance ρ expressed in terms of transport length l^* , (b) I_L, I_R as functions of the source-detector separation for the $\theta_i = 55^\circ, \theta_d = 30^\circ$ setup, (c) the same for the $\theta_i = \theta_d = 0^\circ$ setup, (d) degrees of polarization DoP (red), $DoCP$ (blue), $DoLP$ (green) and corresponding normalized Stokes vector components Q_n, U_n, V_n on the Poincaré sphere for the $\theta_i = 55^\circ, \theta_d = 30^\circ$ setup, (e) the same for the $\theta_i = \theta_d = 0^\circ$ setup, (f) difference between I_L, I_R sampling volumes for the $\theta_i = \theta_d = 0^\circ$ setup and the same source-detector separation distances ρ/l^* as on (a). In these simulations detector with open numerical aperture NA has been considered. Points on the Poincaré spheres are colored gradually from red to yellow, which corresponds to the increase of ρ/l^* distance.

361 point (demarcated by red and blue background colors) the intensities of two streams of light with
 362 opposite helicities are equalized ($I_R = I_L$) and their superposition originates linear polarization.
 363 The polarization memory is revealed as a flip of the backscattered CPL at the source-detector separation
 364 over the transport length ($\rho > l^*$), tailing the helicity of incident RCP light. The resulting
 365 superposition of the scattered RCP and LCP light is registered by the detector as elliptically
 366 polarized light. It should be noted that elliptical polarization can be observed with any non-zero
 367 phase of the incident CPL if the plane of observation is not parallel or perpendicular to the original
 368 vibration direction of the field, which is accounted for in the developed model.

369 We proceed with the analysis of light depolarization by comparing $DoP, DoLP$ and $DoCP$
 370 versus source-detector separation. Corresponding plots are presented in Figures 3d, 3e along with
 371 the normalized Stokes vector components Q_n, U_n, V_n are depicted on the Poincaré sphere. $DoCP$
 372 represents the fraction of the circularly polarized light that is preserved or retained after the multiple
 373 scattering. With the increase of source-detector separation the $DoCP$ is decreased due to reduction
 374 of low scattering orders contribution to the backscattered light. At a particular source-detector
 375 separation where flipped I_L and preserved I_R components of the backscattered circularly polarized
 376 light are equalized (see Figs. 3b and 3c), the $DoCP$ reaches a minimum value. The depolarization
 377 minimum represents the point at which the components of scattered circularly light with opposite
 378 helicity, LCP and RCP , are superimposed. The depolarization minimum is coincided with the

379 demarcation line between non-diffusive and diffusing path lengths of scattering photons charac-
 380 terized by l^* . This phenomenon is well pronounced when utilizing the angular source-detector
 381 configuration (see Figs. 3b, 3d). These results significantly contribute to our understanding of the
 382 depolarization processes within tissues and prove to be useful e.g. for the advanced alignment of
 383 the experimental setup with a conventional polarimeter employed to measure Stokes parameters
 384 and degrees of polarization of the backscattered elliptically polarized light.

385 All data present on the Figure 3 has been computed with open numerical aperture of the detec-
 386 tor ($NA > 70^\circ$). In order to both explore the aperture influence and validate the results towards
 387 experimental data another set of simulations was performed with aperture limited to $NA = 30^\circ$
 388 ensuring that only light photons meeting the condition $\text{acos}(\mathbf{s}_N \cdot \mathbf{s}_d) < NA$ (see Sec. 3.1) are
 389 collected from the sample surface. From Figure 4 we find good agreement of the MC simulations
 390 with experimental measurements performed with the setup described in previous works.⁴⁻⁶ Our
 391 simulation parameters provided in the beginning of the results section are already adjusted to ap-
 392 proximately match the experimental setup configuration. In the experiment, we have carried out
 393 polarization measurements of *RCP* light scattered by thick phantom with known optical properties
 394 ($\mu_s = 4 \text{ mm}^{-1}$, $\mu_a = 0.05 \text{ mm}^{-1}$, $g = 0.8$, $n = 1.46$ at $\lambda = 640 \text{ nm}$).⁶²

395 We observe that limitation of the NA in the model led to the shift of the helicity flip location
 396 towards the source ($\rho/l^* \sim 0.6$ for $NA = 30^\circ$ in Fig. 4a as opposed to $\rho/l^* \sim 0.8$ for open NA in
 397 Fig. 3b). We also notice that, as seen from Figures 3b–3c, vertical source-detector setup leads to the
 398 helicity flip position being shifted away from the source ($\rho/l^* \sim 1$), while angular source-detector
 399 placement causes helicity flip position to shift towards the source ($\rho/l^* \sim 0.8$). In other words, the
 400 larger θ_i and θ_d are, the closer helicity flip is to the source. Alternatively, this can be interpreted in
 401 terms of the medium refractive index n which modifies the effective incident and detection angles
 402 θ_i, θ_d according to Snell refraction law. It should be also pointed out that depolarization compo-
 403 sition of the backscattered CPL varies depending on the properties of turbid tissue-like disperse
 404 medium, such as its scattering characteristics, the size and composition of scattering particles im-
 405 plying different scattering phase functions, and the overall optical density.^{1,8,25,64,65}

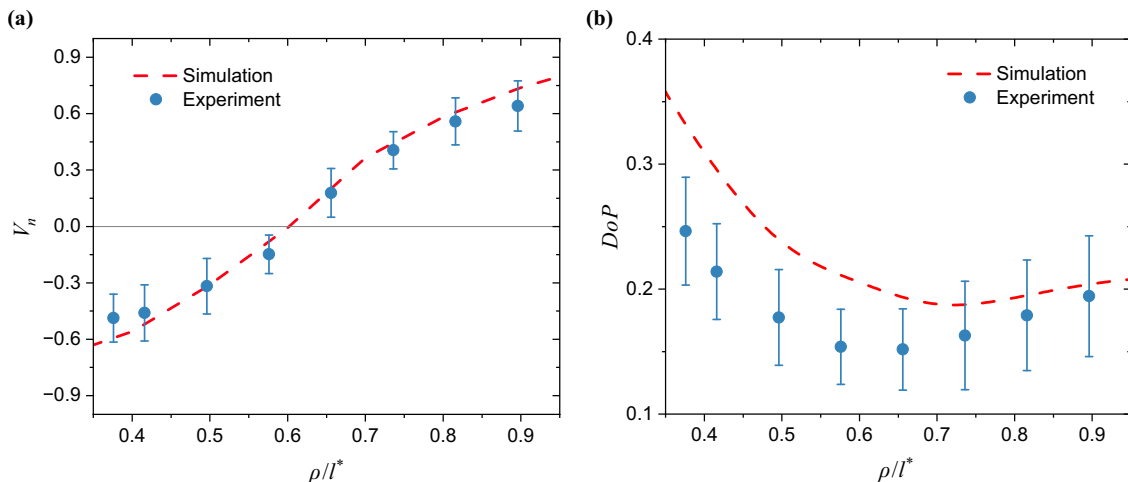


Fig 4 Comparison of (a) the normalized Stokes vector component V_n and (b) the DoP values between the Monte Carlo simulations ($NA = 30^\circ$, $\theta_i = 55^\circ$, $\theta_d = 30^\circ$) and the experimental measurements of tissue-mimicking phantom ($\mu_s = 4 \text{ mm}^{-1}$, $\mu_a = 0.05 \text{ mm}^{-1}$, $g = 0.8$, $n = 1.46$) performed with setup adopted from the previous works.⁴⁻⁶

406 4.3 In-depth spatial distribution of the CPL components and polarization memory

407 Besides analysis of the surface response presented in the previous section, computer simulation
 408 provides an important insight on the in-depth light-tissue interaction. Sampling volume is a tra-
 409 ditional parameter characterizing the detector depth sensitivity. Figures 3a, 3f show 2D maps
 410 computed as difference between sampling volumes (SV) of the oppositely polarized RCP (blue)
 411 and LCP (red) light for several selected dimensionless source-detector separation distances ρ/l^* .
 412 With these maps, we demonstrate that I_R and I_L light portions statistically propagate at different
 413 depths within the sample, as suggested in previous works of A. da Silva.⁶⁶ This result is well pro-
 414 nounced in the angular source-detector configuration (see Fig. 3a). An important outcome is the
 415 possibility to tune the penetration depth of both left- and right-polarized components of light via
 416 adjusting angle and position of the source-detector configuration. It can be clearly seen that prior
 417 to the helicity flip point $I_L > I_R$ (Fig. 3a for $\rho/l^* = 0.4$, Fig. 3f for $\rho/l^* = 0.4, 0.8$), and after
 418 the flip $I_L < I_R$ (Figs. 3a, 3f for $\rho/l^* = 1.2$) in agreement with the results discussed in previous
 419 section. This proves the self-consistency of the proposed MC model and supports the capability of
 420 the model to operate with depolarized light through considering fully polarized orthogonal states.
 421 In this work, sampling volumes have been computed with^{16,17}

$$SV(\mathbf{r}') = \frac{\sum_{j=1}^{N_{ph}} L_j(\mathbf{r}') I_{N_j}}{L_0 \sum_{j=1}^{N_{ph}} I_{N_j}}. \quad (34)$$

422 Here, I_{N_j} corresponds to the detected intensity of the j -th MC-photon defined by the expression
 423 under the sum sign i.e. in (23)–(24), N_{ph} is the amount of detected photons, $L_j(\mathbf{r}')$ is a path length
 424 of the j -th MC-photon within a voxel centered at \mathbf{r}' , L_0 is linear size of the voxel. Evaluation of
 425 (34) provides us with a 3D array $SV(x, y, z)$ depicting detector depth sensitivity within each voxel.
 426 2D maps shown in Figs. 3a, 3f are computed as $SV_R(x, 0, z) - SV_L(x, 0, z)$ with SV_R, SV_L defined
 427 via corresponding I_R, I_L intensities. To the best of our knowledge, this is the first time when the
 428 discussed phenomena of right- and left-polarized light components possessing different sampling
 429 volumes is both quantitatively and qualitatively described with the Monte Carlo simulations.

430 To conclude this section, we point out that within our model it is possible to extensively study
 431 the distribution of polarized light within tissue in terms of polarization extinction ratio (PER).⁶⁷
 432 $P = I_L/I_R$. PER characterizes the extent of polarization cross talk between flipped and preserved
 433 components of the backscattered circularly polarized light. Figure 5 shows the in-depth spatial
 434 distribution of the polarization memory, presented by analogy to the photon-measurement density
 435 function (PMDF),⁶⁸ in terms of gradient of PER computed similarly to the sampling volume in eq.
 436 (34). PER refers to the relative intensities of LCP and RCP components and describes the mixing
 437 of flipped polarization with the orthogonal one as a result of multiple scattering interactions. Fig. 5
 438 shows a strong localization of LCP component in relation to the incident polarization state at the
 439 short ($\rho < l^*$) source-detector distances for both setup configurations. The linear polarization,
 440 emerged as a superposition of LCP and RCP components, demarcates areas of their localization.
 441 The wide aperture of the detector ($NA > 70^\circ$) and anisotropy of scattering g result in a broad
 442 range of scattering angles of photons and their path length distribution, leading to an asymmetry
 443 of the in-depth spatial distribution which is strengthened when both source and detector are not
 444 oriented along the normal to the surface of the turbid medium.

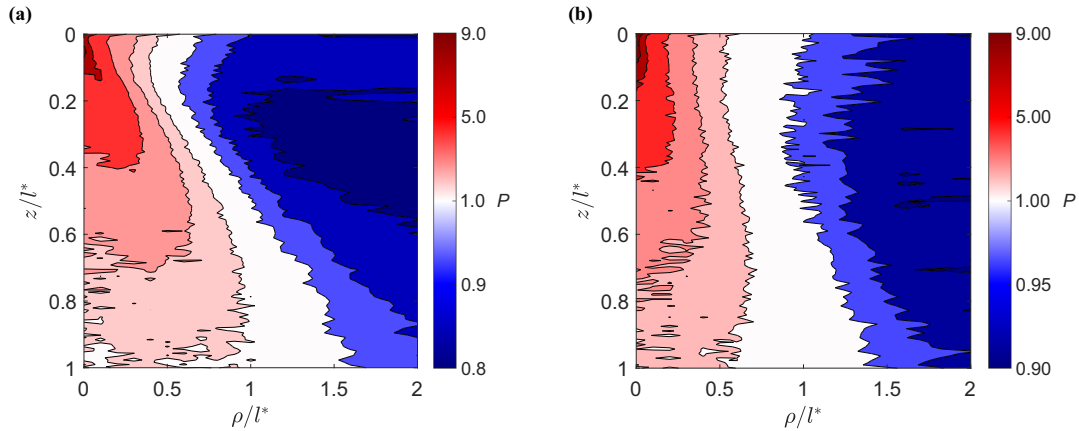


Fig 5 Polarization memory $P = I_L/I_R$ for (a) the angular setup with $\theta_i = 55^\circ, \theta_d = 30^\circ$ and for (b) the vertical setup with $\theta_i = \theta_d = 0^\circ$ as a function of the dimensionless penetration depth z/l^* and source-detector separation ρ/l^* , where l^* is the transport length. Scale step on the colorbar for regions with preserved helicity (blue) is chosen differently from the scale for regions with flipped helicity (red) in order to make the distribution details visible.

445 4.4 Mueller matrix evaluation

446 Finally, in Figure 6 we present an example of Mueller matrix elements computed by (32)–(33).
 447 This data was obtained for the vertically positioned source and detector. Here, the detector reg-
 448 isters the transmitted signal in 1x1 cm area, $\rho = 0$. These results demonstrate that our developed
 449 approach is inherently capable of carrying out Mueller matrix computations. The ability to simu-
 450 late Mueller matrix numerically is especially relevant because most of the experimental research
 451 on interaction of the polarized light with tissues employs Stokes-Mueller formalism as a stan-
 452 dard.^{61,69} As outlined in Sec. 3.4, one of the main advantages of our approach is the ability to
 453 evaluate Mueller matrix without the need to launch multiple simulations for different incident po-
 454 larization states. By presenting the established model in this paper, we aim to further develop our
 455 Mueller matrix Monte Carlo with respect to applications in the course of the subsequent research.

456 5 Conclusion

457 We introduce a Monte Carlo modeling approach which provides combined Jones and Stokes-
 458 Mueller formalism. Our model utilizes the polarization tracing framework based on the itera-
 459 tive solution to Bethe-Salpeter equation. The reflection and refraction of the linearly, elliptical
 460 and/or circularly polarized light at the medium surface are generalized and properly included in
 461 the model. Self-consistency of the proposed model is ensured by the developed theoretical frame-
 462 work and confirmed by both numerical experiments and phantom measurements. One of the main
 463 advantages of the proposed approach is the ability to evaluate Mueller matrix elements, as well as
 464 other characteristics like sampling volumes or degrees of polarization, with single simulation.

465 The results of modeling studies reveal the origins of the experimentally observed helicity flip
 466 that depends both on the configuration of the source-detector setup and turbid medium properties.
 467 Firstly, we have shown that for the CPL backscattered from the turbid medium the flipped helicity
 468 survival is prevailed at the short source-detector separation ($\rho < l^*$). A transition from *LCP* to
 469 *RCP* is revealed for longer distances ($\rho > l^*$) resulting in preservation of the helicity of inci-
 470 dent light. Secondly, we have demonstrated that backscattered CPL within MC is appropriately
 471 decomposed into two fully polarized orthogonal components with opposite helicities, and their

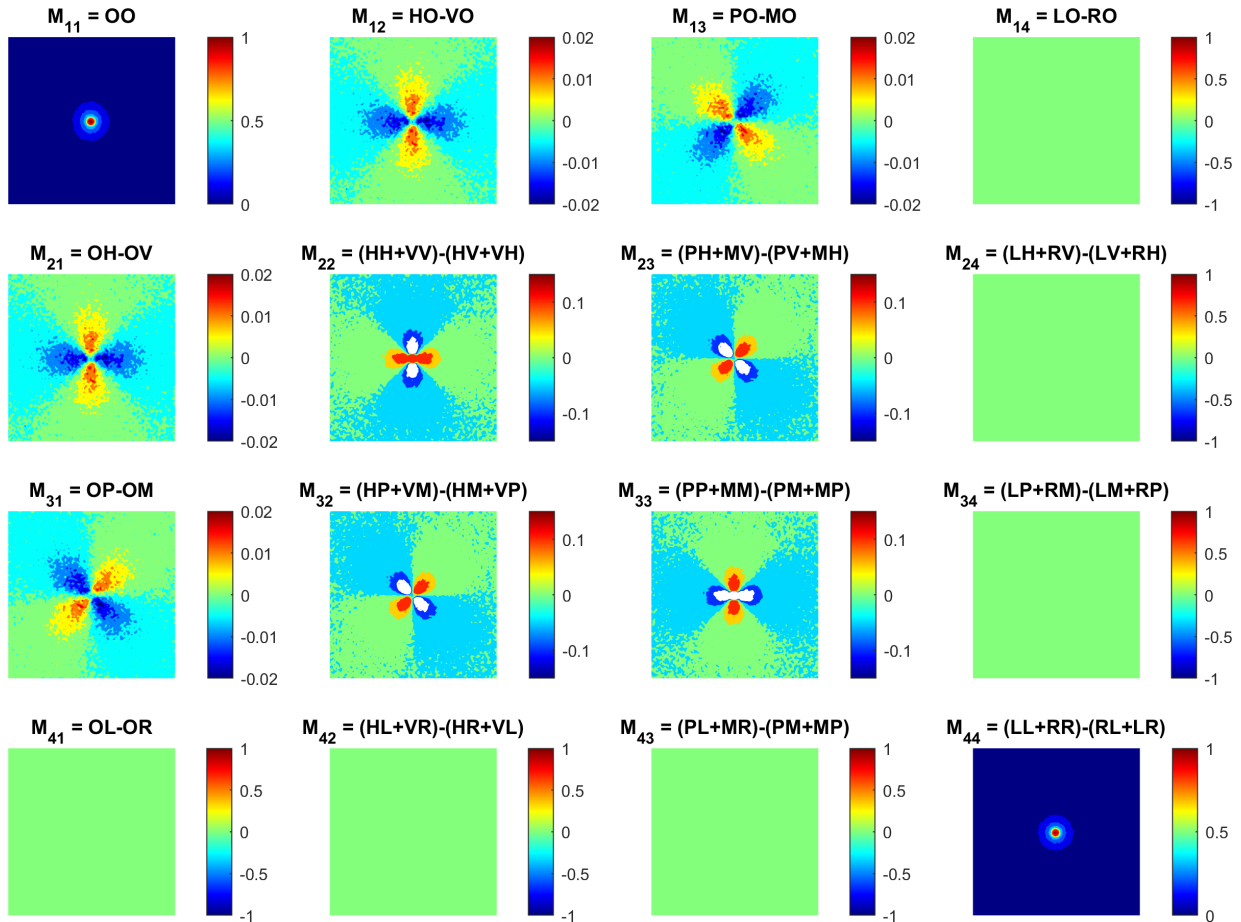


Fig 6 Mueller matrix elements obtained by Monte Carlo modeling for turbid scattering medium with the following optical properties: $\mu_s = 1 \text{ mm}^{-1}$, $\mu_a = 0.01 \text{ mm}^{-1}$, $g = 0.74$, $n = 1.33$. Here, detector registers the signal transmitted through medium with 4 mm thickness. The dimension of each image is 1x1 cm, which is equal to the detector size. The individual images are represented by a two-letter combination that denotes the input polarization and the output analyzer orientation as defined in (31).

472 polarization state is fully defined. Thirdly, we have reported on the different penetration depth of
 473 *RCP* and *LCP* light as demonstrated by the sampling volume simulations. And finally, we have
 474 addressed the in-depth binding of circular polarization memory with the helicity flips occurring
 475 within the medium.

476 It should be pointed out that developed MC framework is suitable to imitate light beams of
 477 different shapes, such as traditional point sources, plane waves, Gaussian and Bessel beams, as
 478 well as complex laser beams carrying orbital angular momentum (e.g. Laguerre-Gaussian) via
 479 appropriate definition of the initial MC-photon intensity and direction distributions. In addition,
 480 diverse source-detector configurations, coherent properties of incident light and arbitrary polariza-
 481 tion states can be taken into account without further modifications of the code core components.

482 In summary, the combined use of Jones and Stokes-Mueller formalisms in MC modeling offers
 483 benefits such as comprehensive polarization modeling, flexibility in simulating different optical
 484 elements, accurate representation of complex optical systems, validation against experimental data,
 485 and enhanced understanding of polarization phenomena. These advantages make this approach
 486 valuable in a wide range of fields, including biomedical optics, remote sensing, atmospheric optics,

487 and more.

488 *Disclosures*

489 No conflicts of interest, financial or otherwise, are declared by the authors.

490 *Acknowledgments*

491 Authors acknowledge the support from ATTRACT II META-HiLight project funded by the Eu-
492 ropean Union’s Horizon 2020 research and innovative programme under grant agreement No.
493 101004462, the Academy of Finland (grant project 325097), the Leverhulme Trust and The Royal
494 Society (Ref. no.: APX111232 APEX Awards 2021).

495 *Data, Materials, and Code Availability*

496 Data underlying the results is available from the corresponding author upon reasonable request.

497 *References*

- 498 1 M. Singh and I. Vitkin, “Spatial helicity response metric to quantify particle size and turbidity
499 of heterogeneous media through circular polarization imaging,” *Sci. Rep.* **13**, 2231 (2023).
500 [doi:10.1038/s41598-023-29444-9].
- 501 2 M. Peyvasteh, A. Dubolazov, A. Popov, *et al.*, “Two-point Stokes vector diagnostic approach
502 for characterization of optically anisotropic biological tissues,” *J. Phys. D: Appl. Phys.* **53**,
503 395401 (2020). [doi:10.1088/1361-6463/ab9571].
- 504 3 A. Ushenko, A. Sdobnov, A. Syvokorovskaya, *et al.*, “Stokes-correlometry analysis of biolog-
505 ical tissues with polycrystalline structure,” *IEEE J. Sel. Top. Quantum Electron.* **25**, 7101612
506 (2019). [doi:10.1109/JSTQE.2018.2865443].
- 507 4 M. Borovkova, O. Sieryi, I. Lopushenko, *et al.*, “Screening of Alzheimer’s disease with mul-
508 tiwavelength Stokes polarimetry in a mouse model,” *IEEE Trans. Med. Imaging* **41**, 977–982
509 (2022). [doi:10.1109/tmi.2021.3129700].
- 510 5 M. Borovkova, A. Bykov, A. Popov, *et al.*, “Evaluating β -amyloidosis progression in
511 Alzheimer’s disease with Mueller polarimetry,” *Biomed. Opt. Express* **11**, 4509–4519 (2020).
512 [doi:10.1364/boe.396294].
- 513 6 D. Ivanov, V. Dremin, A. Bykov, *et al.*, “Colon cancer detection via Poincaré sphere represen-
514 tation and 2D polarimetric mapping of *ex vivo* tissue samples,” *J. Biophoton.* **13**, e202000082
515 (2020). [doi:10.1002/jbio.202000082].
- 516 7 B. Kunnen, C. Macdonald, A. Doronin, *et al.*, “Application of circularly polarized light for
517 non-invasive diagnosis of cancerous tissues and turbid tissue-like scattering media,” *J. Bio-*
518 *photonics* **8**, 317 – 323 (2015). [doi:10.1002/jbio.201400104].
- 519 8 C. M. Macdonald, S. L. Jacques, and I. V. Meglinski, “Circular polarization
520 memory in polydisperse scattering media,” *Phys. Rev. E* **91**, 033204 (2015).
521 [doi:10.1103/PhysRevE.91.033204].
- 522 9 J. C. Ramella-Roman, I. Saytashev, and M. Piccini, “A review of polarization-based imag-
523 ing technologies for clinical and preclinical applications,” *J. Opt.* **22**, 123001 (2020).
524 [doi:10.1088/2040-8986/abfb8a].

- 525 10 Q. Fang, F. Martelli, and L. Lilge, “Special Section Guest Editorial: Introduction to the
526 Special Section Celebrating 30 years of Open Source Monte Carlo Codes in Biomedical
527 Optics,” *J. Biomed. Opt.* **27**, 083001 (2022). [doi:10.1117/1.JBO.27.8.083001].
- 528 11 N. Nishizawa and T. Kuchimaru, “Depth estimation of tumor invasion in early gastric cancer
529 using scattering of circularly polarized light: Monte Carlo simulation study,” *J. Biophotonics*
530 **15**, e202200062 (2022). [doi:10.1002/jbio.202200062].
- 531 12 V. Periyasamy and M. Pramanik, “Advances in Monte Carlo simulation for
532 light propagation in tissue,” *IEEE Rev. Biomed. Eng.* **10**, 125 – 135 (2017).
533 [doi:10.1109/RBME.2017.2739801].
- 534 13 A. Doronin, L. Tchvialeva, I. Markhvida, *et al.*, “Backscattering of linearly polarized light
535 from turbid tissue-like scattering medium with rough surface,” *J. Biomed. Opt.* **21**, 071117
536 (2016). [doi:10.1117/1.jbo.21.7.071117].
- 537 14 A. Doronin, C. Macdonald, and I. Meglinski, “Propagation of coherent polar-
538 ized light in highly scattering turbid media,” *J. Biomed. Opt.* **19**, 025005 (2014).
539 [doi:10.1117/1.jbo.19.2.025005].
- 540 15 L. Wang, S. L. Jacques, and L. Zheng, “MCML—Monte Carlo modeling of light trans-
541 port in multi-layered tissues,” *Comput. Methods Programs Biomed.* **47**, 131–146 (1995).
542 [doi:10.1016/0169-2607(95)01640-F].
- 543 16 I. V. Meglinski and S. J. Matcher, “Modelling the sampling volume for skin blood oxygena-
544 tion measurements,” *Med. Biol. Eng. Comput.* **39**, 44–50 (2001). [doi:10.1007/BF02345265].
- 545 17 I. Meglinski, A. N. Bashkatov, E. A. Genina, *et al.*, “Study of the possibility of in-
546 creasing the probing depth by the method of reflection confocal microscopy upon immer-
547 sion clearing of near-surface human skin layers,” *Quantum Electron.* **32**, 875–882 (2002).
548 [doi:10.1070/QE2002v032n10ABEH002309].
- 549 18 V. V. Tuchin, *Tissue Optics: Light Scattering Methods and Instruments for Medical Diagnos-*
550 *tics*, SPIE Press, Bellingham, Washington, 3rd ed. (2015). [doi:10.1117/3.1003040].
- 551 19 I. Meglinski and A. Doronin in *Advanced Biophotonics: Tissue Optical Sectioning*,
552 R. K. Wang and V. V. Tuchin, Eds., ch. 1, 1–72, CRC Press, Boca Raton (2013).
553 [doi:10.1201/b15256].
- 554 20 A. Sassaroli and F. Martelli, “Equivalence of four Monte Carlo methods for photon migration
555 in turbid media,” *J. Opt. Soc. Am. A* **29**, 2110–2117 (2012). [doi:10.1364/JOSAA.29.002110].
- 556 21 T. Novikova, I. Meglinski, J. C. Ramella-Roman, *et al.*, “Polarized light for biomedical ap-
557 plications,” *J. Biomed. Opt.* **21**, 071001 (2016). [doi:10.1117/1.JBO.21.7.071001].
- 558 22 I. Meglinski, T. Novikova, and K. Dholakia, “Polarization and orbital angular momentum of
559 light in biomedical applications: feature issue introduction,” *Biomed. Opt. Express* **12**, 6255
560 – 6258 (2021). [doi:10.1364/BOE.442828].
- 561 23 J. C. Ramella-Roman, S. A. Prahl, and S. L. Jacques, “Three Monte Carlo programs of po-
562 larized light transport into scattering media: part I,” *Opt. Express* **13**, 4420–4438 (2005).
563 [doi:10.1364/OPEX.13.004420].
- 564 24 J. C. Ramella-Roman, S. A. Prahl, and S. L. Jacques, “Three Monte Carlo programs of po-
565 larized light transport into scattering media: part II,” *Opt. Express* **13**, 10392–10405 (2005).
566 [doi:10.1364/OPEX.13.010392].

- 567 25 A. H. Hielscher, J. R. Mourant, and I. J. Bigio, "Influence of particle size and concentra-
568 tion on the diffuse backscattering of polarized light from tissue phantoms and biological cell
569 suspensions," *Appl. Opt.* **36**, 125–135 (1997). [doi:10.1364/AO.36.000125].
- 570 26 S. Bartel and A. H. Hielscher, "Monte Carlo simulations of the diffuse backscatter-
571 ing Mueller matrix for highly scattering media," *Appl. Opt.* **39**, 1580–1588 (2000).
572 [doi:10.1364/AO.39.001580].
- 573 27 X. Wang and L. V. Wang, "Propagation of polarized light in birefringent turbid media: time-
574 resolved simulations," *Opt. Express* **9**, 254–259 (2001). [doi:10.1364/OE.9.000254].
- 575 28 M. Xu, "Electric field Monte Carlo simulation of polarized light propagation in turbid media,"
576 *Opt. Express* **12**, 6530–6539 (2004). [doi:10.1364/OPEX.12.006530].
- 577 29 M. I. Mishchenko, "Vector radiative transfer equation for arbitrarily shaped and arbitrarily
578 oriented particles: a microphysical derivation from statistical electromagnetics," *Appl. Opt.*
579 **41**, 7114–7134 (2002). [doi:10.1364/AO.41.007114].
- 580 30 M. J. Raković, G. W. Kattawar, M. Mehrúbeoğlu, *et al.*, "Light backscattering polariza-
581 tion patterns from turbid media: theory and experiment," *Appl. Opt.* **38**, 3399–3408 (1999).
582 [doi:10.1364/AO.38.003399].
- 583 31 H. H. Tynes, G. W. Kattawar, E. P. Zege, *et al.*, "Monte Carlo and multicomponent approxi-
584 mation methods for vector radiative transfer by use of effective Mueller matrix calculations,"
585 *Appl. Opt.* **40**, 400–412 (2001). [doi:10.1364/AO.40.000400].
- 586 32 E. Akkermans, P. E. Wolf, R. Maynard, *et al.*, "Theoretical study of the coher-
587 ent backscattering of light by disordered media," *J. Phys. France* **49**, 77–98 (1988).
588 [doi:10.1051/jphys:0198800490107700].
- 589 33 I. Meglinski, V. L. Kuzmin, D. Y. Churmakov, *et al.*, "Monte Carlo simulation
590 of coherent effects in multiple scattering," *Proc. R. Soc. A* **463**, 43 – 53 (2005).
591 [doi:10.1098/rspa.2004.1369].
- 592 34 V. L. Kuz'min and I. V. Meglinskiĭ, "Backscattering of linearly and circularly polar-
593 ized light in randomly inhomogeneous media," *Opt. Spectrosc.* **106**, 257–267 (2009).
594 [doi:10.1134/S0030400X09020180].
- 595 35 I. Meglinski and V. L. Kuz'min, "Coherent backscattering of circularly polarized optical
596 radiation from a disperse random medium," *Prog. Electromagn. Res. M* **21**, 1972 — 1977
597 (2011). [doi:10.2528/PIERM10102106].
- 598 36 A. Doronin, A. Radosevich, V. Backman, *et al.*, "Two electric field Monte Carlo models
599 of coherent backscattering of polarized light," *J. Opt. Soc. Am. A* **31**, 2394–2400 (2014).
600 [doi:10.1364/JOSAA.31.002394].
- 601 37 S. V. Gangnus, S. J. Matcher, and I. Meglinski, "Monte Carlo modeling of po-
602 larized light propagation in biological tissues," *Laser Phys.* **14**(6), 886–891 (2004).
603 <https://www.semanticscholar.org/>.
- 604 38 V. L. Kuzmin and I. Meglinski, "Anomalous polarization phenomena during
605 light scattered in random media," *J. Exp. Theor. Phys.* **137**, 742–753 (2010).
606 [doi:10.1134/S1063776110050031].
- 607 39 V. L. Kuzmin and I. V. Meglinski, "Dependence of the circular polarization of backscat-
608 tered light in random media on anisotropy of scatterers," *Opt. Spectrosc.* **108**, 99–106 (2010).
609 [doi:10.1134/S0030400X10010157].

- 610 40 A. Doicu and M. I. Mishchenko, “An overview of methods for deriving the radiative transfer theory from the Maxwell equations. II: Approach based on the Dyson and
611 Bethe–Salpeter equations,” *J. Quant. Spectrosc. Radiat. Transfer* **224**, 25–36 (2019).
612 [doi:10.1016/j.jqsrt.2018.10.032].
613
- 614 41 S. Yan, S. L. Jacques, J. C. Ramella-Roman, *et al.*, “Graphics-processing-unit-accelerated
615 Monte Carlo simulation of polarized light in complex three-dimensional media,” *J. Biomed.
616 Opt.* **27**, 083015 (2022). [doi:10.1117/1.JBO.27.8.083015].
- 617 42 H. G. Akarçay, A. Hohmann, A. Kienle, *et al.*, “Monte Carlo modeling of polarized
618 light propagation: Stokes vs Jones - Part I,” *Appl. Opt.* **53**, 7576 – 7585 (2014).
619 [doi:10.1364/AO.53.007576].
- 620 43 D. Goldstein, *Polarized light*, Marcel Dekker, New York (2003).
- 621 44 F. C. MacKintosh, J. X. Zhu, D. J. Pine, *et al.*, “Polarization memory of multiply scattered
622 light,” *Phys. Rev. B* **40**, 9342–9345 (1989). [doi:10.1103/PhysRevB.40.9342].
- 623 45 M. Xu and R. R. Alfano, “Circular polarization memory of light,” *Phys. Rev. E* **72**, 065601
624 (2005). [doi:10.1103/physreve.72.065601].
- 625 46 Y. L. Kim, P. Pradhan, M. H. Kim, *et al.*, “Circular polarization memory effect in
626 low-coherence enhanced backscattering of light,” *Opt. Lett.* **31**, 2744 – 2746 (2006).
627 [doi:10.1364/OL.31.002744].
- 628 47 A. Bykov, A. Doronin, and I. Meglinski in *Deep Imaging in Tissue and Biomedical Materials:
629 Using Linear and Nonlinear Optical Methods*, L. Shi and R. Alfano, Eds., ch. 9, 295–322,
630 Pan Stanford Publishing, Singapore (2017). [doi:10.1201/9781315206554].
- 631 48 M. Born and E. Wolf, *Principles of Optics*, Cambridge University Press (2019).
- 632 49 Thorlabs GmbH, Bergkirchen, Germany, *Compact Polarimeter PAX1000 Operation Manual*
633 (2022). <https://www.thorlabs.com/>.
- 634 50 M. V. Berry and K. T. McDonald, “Exact and geometrical optics energy trajectories in
635 twisted beams,” *J. Opt. A: Pure Appl. Opt.* **10**(3), 035005 (2008). [doi:10.1088/1464-
636 4258/10/3/035005].
- 637 51 I. Lopushenko, A. Sdobnov, A. Bykov, *et al.*, “Propagation of shaped light carrying
638 orbital angular momentum through turbid tissue-like scattering medium,” in
639 *2023 CLEO/Europe-EQEC Conference Abstracts*, (2023). [doi:10.1109/CLEO/Europe-
640 EQEC57999.2023.10231893].
- 641 52 L. G. Henyey and J. L. Greenstein, “Diffuse radiation in the Galaxy,” *Astrophys. J.* **93**, 70–83
642 (1941). [doi:10.1086/144246].
- 643 53 D. Toublanc, “Henyey–Greenstein and Mie phase functions in Monte Carlo radiative transfer
644 computations,” *Appl. Opt.* **35**, 3270–3274 (1996). [doi:10.1364/AO.35.003270].
- 645 54 Y. Fu and S. L. Jacques, “Monte Carlo simulation study on phase function,” in *Optical Interactions with Tissue and Cells XVII*, S. L. Jacques and W. P. Roach, Eds., *Proc. SPIE* **6084**,
646 608408 (2006). [doi:10.1117/12.657490].
647
- 648 55 V. V. Tuchin, Ed., *Handbook of Optical Biomedical Diagnostics, Second Edition, Volume 1: Light-Tissue Interaction*, SPIE Press, Bellingham, Washington, USA (2016).
- 649
650 56 V. Kuz'min, A. Val'kov, and L. Zubkov, “Photon diffusion in random media and anisotropy
651 of scattering in the Henyey–Greenstein and Rayleigh–Gans models,” *J. Exp. Theor. Phys.*
652 **128**, 396–406 (2019). [doi:10.1134/S1063776119020109].

- 653 57 C. F. Bohren and D. R. Huffman, *Absorption and Scattering of Light by Small Particles*,
654 Wiley (1983).
- 655 58 A. Ishumar, *Wave Propagation and Scattering in Random Media*, Academic Press, New
656 York (1978).
- 657 59 M. A. Borovkova, A. V. Bykov, A. Popov, *et al.*, “Role of scattering and birefringence in
658 phase retardation revealed by locus of Stokes vector on Poincaré sphere,” *J. Biomed. Opt.* **25**,
659 057001 (2020). [doi:10.1117/1.JBO.25.5.057001].
- 660 60 A. H. Hielscher, A. A. Eick, J. R. Mourant, *et al.*, “Diffuse backscattering Mueller matrices
661 of highly scattering media,” *Opt. Express* **1**, 441–453 (1997). [doi:10.1364/OE.1.000441].
- 662 61 T. Novikova and J. C. Ramella-Roman, Eds., *Polarized Light in Biomedical Imaging and
663 Sensing: Clinical and Preclinical Applications*, Springer (2022).
- 664 62 O. Sieryi, A. Popov, V. Kalchenko, *et al.*, “Tissue-mimicking phantoms for biomedical ap-
665 plications,” in *Tissue Optics and Photonics*, V. V. Tuchin, W. Blondel, and Z. Zalevsky, Eds.,
666 *Proc. SPIE* **11363**, 1136312 (2020). [doi:10.1117/12.2560174].
- 667 63 A. D. Kim and M. Moscoso, “Influence of the relative refractive index on the
668 depolarization of multiply scattered waves,” *Phys. Rev. E* **64**, 026612 (2001).
669 [doi:10.1103/PhysRevE.64.026612].
- 670 64 L. F. Rojas-Ochoa, D. Lacoste, R. Lenke, *et al.*, “Depolarization of backscattered linearly
671 polarized light,” *J. Opt. Soc. Am. A* **21**, 1799–1804 (2004). [doi:10.1364/JOSAA.21.001799].
- 672 65 D. Bicout, C. Brosseau, A. S. Martinez, *et al.*, “Depolarization of multiply scattered waves
673 by spherical diffusers: Influence of the size parameter,” *Phys. Rev. E* **49**, 1767 – 1770 (1994).
674 [doi:10.1103/PhysRevE.49.1767].
- 675 66 S. Sridhar and A. da Silva, “Enhanced contrast and depth resolution in polariza-
676 tion imaging using elliptically polarized light,” *J. Biomed. Opt.* **21**, 071107 (2016).
677 [doi:10.1117/1.JBO.21.7.071107].
- 678 67 R. M. Azzam and N. M. Bashara, *Ellipsometry and Polarized Light*, Elsevier, New York
679 (1989).
- 680 68 S. R. Arridge, “Photon-measurement density functions. Part I: Analytical forms,” *Appl. Opt.*
681 **34**, 7395–7409 (1995). [doi:10.1364/AO.34.007395].
- 682 69 T. Novikova and J. C. Ramella-Roman, “Is a complete Mueller matrix necessary in biomed-
683 ical imaging?,” *Opt. Lett.* **47**(21), 5549–5552 (2022). [doi:10.1364/OL.471239].